J. Fluid Mech. (2004), *vol.* 500, *pp.* 1–27.
DOI: 10.1017/S0022112003006396 Printed in the United Kingdom

Size, shape and dynamics of large-scale turbulent flow structures in a gravel-bed river

By ANDRÉ G. ROY[1], THOMAS BUFFIN-BÉLANGER[2], HÉLÈNE LAMARRE[1] AND ALISTAIR D. KIRKBRIDE[1]

[1]Département de géographie, Université de Montréal, C.P. 6128 Succursale Centre-Ville, Montréal, Québec, H3C 3J7, Canada
andre.roy@umontreal.ca

[2]Module de géographie, Département des Sciences humaines, Université du Québec à Rimouski, 300 allee des Ursulines, Rimouski (Québec), G5L 3A1, Canada

(Received 7 February 2002 and in revised form 11 May 2003)

In this paper, we present a detailed investigation of the size, scale and dynamics of macro-turbulent flow structures in gravel-bed rivers. We used an array of seven electromagnetic current meters with high resolution in both space and time to measure the streamwise velocity fluctuations in a gravel-bed river. The array was deployed successively in various configurations in order to quantify the vertical, lateral and longitudinal extent of the flow structures and to estimate their advecting velocities. To depict the spatial and temporal properties of the flow structures, we used space–time velocity matrices, space–time correlation analysis and coherent-structure detection schemes. The results show that the large-scale turbulent flow structures in a gravel-bed river occupy the entire depth of the flow and that they are elongated and narrow. The length of the structures is 3 to 5 times the flow depth while the width is between 0.5 and 1 times flow depth. In spite of the high roughness of the bed, these values are similar to those reported in the literature for laboratory experiments on large-scale turbulent flow structures. The dynamics of the large-scale turbulent flow structures investigated using flow visualization highlight the interactions between the outer flow region and the near-bed region. Our evidence suggests that large-scale flow incursions trigger ejections in the near-bed region that can develop into megabursts that can reach the water surface.

1. Introduction

The presence of coherent turbulent flow structures at a broad range of spatial and temporal scales has long been recognized in rivers (Matthes 1947; Jackson 1976). Inspired by experimental studies on the coherent turbulent flow structures in boundary layers (see Kline *et al.* 1967; Corino & Brodkey 1969; Offen & Kline 1975), Jackson (1976) examined the duration and frequency of boils at the surface of river flows and speculated on the role of large-scale coherent flow structures in sediment transport and bedform development. In spite of this early recognition, the role of large-scale turbulent flow structures in rivers remains elusive.

In the turbulent boundary layer, coherent flow structures exist in the form of low-speed streaks, ejections and sweeps that comprise the bursting process in the inner region and of large-scale structures in the outer region. These structures were first identified through flow visualization (Kline *et al.* 1967; Grass 1971; Falco 1977) and

	Flow type	*Re*	Length	Width	Height
Blackwelder & Kovasznay (1972)	air	27500[1]	1.1δ[4]		
Falco (1977)	air	1000–4000[2]	1.6δ		
Brown & Thomas (1977)	air	10160[2]	2δ		
Nakagawa & Nezu (1981)	water	4200–12000[3]	$1.5Y$		(0.5–1) Y
Imamoto & Ishigaki (1987)	water	6100–7800[3]	$2Y$	Y	Y
Komori *et al.* (1989)	water	11000[3]	$2Y$	Y	$0.5Y$
Yalin (1992)	water	Not given	$6Y$	$2Y$	Y
Schvidchenko & Pender (2001)	water	12000–98000[3]	(4–5)Y	$2Y$	Y
Liu *et al.* (2001)	water	10756–59870[3]	(1–2)Y		$0.25Y$

[1] Based on the boundary layer thickness (δ). [2] Based on the momentum thickness (θ).
[3] Based on flow depth (Y). [4] Estimated from figure.

TABLE 1. Dimensions of large-scale flow structures from laboratory experiments expressed as a function of boundary layer thickness (δ) or flow depth (Y) for flows at different Reynolds numbers.

they have been studied extensively in the laboratory (Robinson 1991; Falco 1991). Because of their scale, the structures found in the outer region of the turbulent boundary layer are of particular significance for river systems with rough boundaries. Through laboratory experiments, the scales of such macro-turbulent flow structures have been assessed using a variety of means, including flow visualization (Falco 1977; Pratury & Brodkey 1978; Roy & Blackwelder 1994; Tamburrino & Gulliver 1999; Schvidchenko & Pender 2001), cross-correlation analyses of simultaneous velocity measurements (Favre, Gaviglio & Dumas 1957; Brown & Thomas 1977; Nakagawa & Nezu 1981) and more recently, from particle image velocimetry (Liu, Adrian & Hanratty 2001). Table 1 summarizes the characteristic scales obtained from the literature for these large structures. These data were compiled from experiments conducted in air and water flows over smooth boundaries at a wide range of Reynolds numbers. Despite the diverse flow conditions and methods used to estimate the scales of the structures, the similarity among various estimates of the size of the structures is striking: structures are typically twice as long as the flow depth and their lateral and vertical extent is more or less equal to one flow depth. The origin and dynamics of these structures are still under debate, however. In flows over a smooth bed, some authors have argued that the large-scale flow structures are generated in the near-bed region and that they are formed by the expansion and amalgamation of individual bursting motions (Falco 1977; Brown & Thomas 1977; Komori, Murakami & Ueda 1989; Nezu & Nakagawa 1993; Kim & Adrian 1999). Other researchers seem to believe that the large-scale flow structures act as a trigger for the bursting cycle (Laufer 1975; Pratury & Brodkey 1978; Yalin 1992; Roy & Blackwelder 1994). A definite conclusion to this debate might be difficult to reach because both processes are likely to occur.

Very few studies have examined the characteristics of large-scale coherent flow structures in natural rivers where beds are very rough. This is due to the difficulty of collecting high-quality turbulence data in these environments. In recent years, the deployment of multiple velocity sensors has allowed researchers to report and document the presence of macro-turbulent flow structures in gravel-bed and sand-bed rivers. In gravel-bed rivers, large-scale coherent flow structures take the form of intermittent regions of high and low velocity that extend over the entire depth of the

flow (Kirkbride & Ferguson 1995; Ferguson, Kirkbride & Roy 1996; Roy, Buffin-Bélanger & Deland 1996; Dinehart 1999; Buffin-Bélanger, Roy & Kirkbride 2000*a*; Roy & Buffin-Bélanger 2001; Smart 2001). These regions, described as low-speed and high-speed wedges because of their oblique shape, have similarities with the ejections and sweeps that are characteristic of the bursting process in the turbulent boundary layer. This is consistent with earlier observations by Grass (1971) and Grass, Stuart & Mansour-Tehrani (1991) in turbulent boundary layers above homogeneous rough beds. Dinehart (1999) has associated the presence of large velocity fluctuations with the movement of gravel bedforms while Buffin-Bélanger *et al.* (2000*a*) have suggested a close relationship between the passage of high-speed wedges and peaks in shear stress applied at the river bed. This suggestion is in agreement with the correlation between sediment transport events and strong flow events belonging to the first and fourth quadrants of turbulent motions observed by Nelson *et al.* (1995) and by Niño & Garcia (1996) and with the increased movement of bed particles following the advection of a high-speed region reported by Schvidchenko & Pender (2001). Furthermore, it seems that eddy shedding in the lee of pebble clusters and of large protruding particles takes different forms according to the type of wedge that passes over the obstacle (Roy *et al.* 1999; Buffin-Bélanger, Roy & Levasseur 2001). This relationship between large-scale flow structures and shedding is important for the understanding of flow resistance over a rough bed. Shedding of vortices downstream from protruding clasts in gravel-bed rivers has been identified as the most significant process by which the energy is dissipated within a river flow (Robert, Roy & De Serres 1996; Buffin-Bélanger & Roy 1998).

Our understanding of the flow organization at the river reach scale and of its effect on fluvial dynamics depends upon our ability to characterize the macro-turbulent structures in river flows (Buffin-Bélanger, Roy & Kirkbride 2000*b*). It is clear, however, that large-scale turbulent flow structures have not yet been described and characterized in significant detail for a clear assessment of their role in fluvial dynamics. As a consequence, knowledge on the large-scale turbulent flow structures in rivers is very limited and there is a need for a detailed study that will directly investigate the longitudinal and lateral extent, the spatial persistence and the dynamics of the large-scale turbulent flow structures in natural rivers. The objective of this paper is to present new evidence that will fulfil this need by quantifying the size and shape of the macro-turbulent flow structures found in a gravel-bed river. To achieve this goal, we have implemented in a river flow a research design that mimics those used in laboratory experiments. We have deployed simultaneously several current meters in various spatial configurations and analysed velocity records measured at a high spatial and temporal resolution using cross-correlation techniques. The experiment also relied on flow visualization to examine the dynamics of the flow structures.

2. Methods

2.1. *Instrumentation and sampling design*

The experiments were carried out in the Eaton-North River, Québec, Canada (figure 1). At the time of sampling, the selected reach had an average width of 17 m. In the experiments, the maximum flow depths ranged between 35 and 60 cm with average velocities from 67 to 45 cm s^{-1}. The Reynolds number was between 150 000 and 200 000. The bed was composed of well imbricated cobbles and gravel, with D_{50} ranging between 30 and 45 mm. The particles of the bed are poorly sorted (sorting coefficient ~ 3, where the coefficient is defined as $(D_{84} - D_{16})/4 + (D_{95} - D_5)/6.6$

FIGURE 1. An upstream view of the study reach on the Eaton-North River, Québec, Canada.

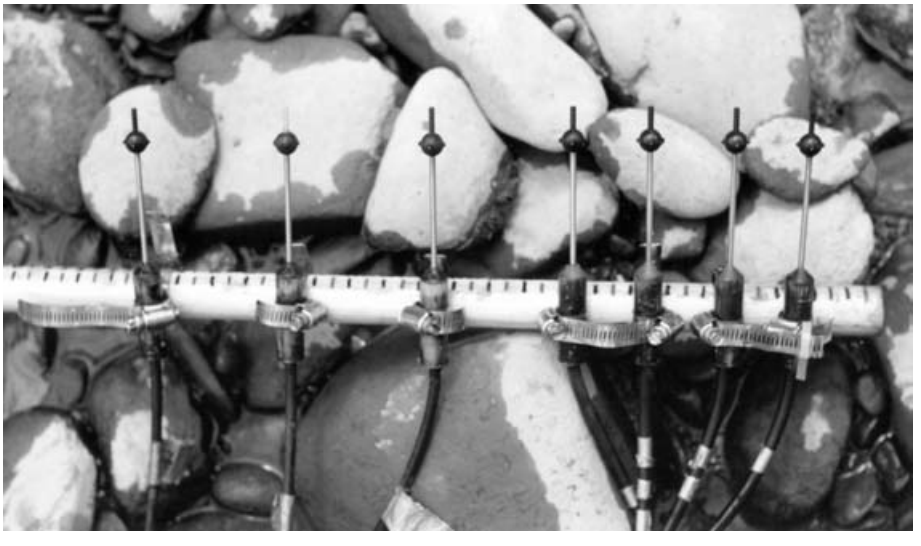

FIGURE 2. Seven Marsh-McBirney bidirectional electromagnetic current meters model 523 mounted on a wading rode for the vertical deployment.

in which D_x represents the diameter of the xth percentile obtained from the distribution of bed particles, in ϕ units (Folk 1974). The field experiment was carried out in a period of eight hours on a single day. The discharge of the river was low and it remained constant during the experiment. Flow stage did not fluctuate by more than 1 cm during the experiment.

Seven bi-directional electromagnetic current meters (ECM) were used to measure velocity fluctuations (figure 2). This type of instrument is frequently used in field studies because of its reliability and robustness. The Marsh-McBirney 523 used in

this study allows sampling at the highest spatial and temporal resolutions for that type of instrument. An ECM sensor uses the Faraday principle that a fluid passing through a magnetic field generates a voltage that is proportional to its velocity. In the Marsh-McBirney sensors, an electromagnetic field is generated by a magnet that is energized at a frequency of 50 Hz. Two pairs of electrodes disposed orthogonally on a small sphere that is 1.3 cm in diameter are used to capture the voltages. The sensor can measure two velocity components simultaneously. The sensing volume around the probe has a diameter two to three times larger than that of the sphere. The response time of the instrument is 0.05 s giving a half-power of 3.18 Hz. Instantaneous voltages are passed through a RC filter. The voltages are collected in a datalogger (Cambpell 21x). The seven sensors were operated simultaneously. However, due to the limited number of input channels (8) on the datalogger, only one velocity component, in this case the streamwise component, could be sampled when all seven current meters were deployed at once. Sampling frequency was 20 Hz.

In order to quantify the vertical, longitudinal and lateral extent of the flow structures, three different deployment strategies were carried out. To determine the vertical extent of the flow structures, the ECMs were fixed on a wading rod at heights of 5, 9, 13, 17, 25, 33, and 41 cm above the bed (figure 2). Five velocity profiles were sampled along a transect at locations having flow depths ranging from 46 to 59 cm. Streamwise velocities were sampled simultaneously by each ECM for a duration of two minutes. For the longitudinal extent, the ECMs were fixed on a rod with a separation distance of 30 cm between each sensor (figure 3*a*). The rod was attached above the water surface and parallel to the flow streamlines. The sensor heads were located 9.5 cm beneath the water surface in a flow with an average depth of 32 cm. Streamwise velocities were measured for 20 minutes. The separation distance of 30 cm was selected because it is nearly equal to flow depth. At this distance, the effect of a sensor on the turbulent flow characteristics of its downstream neighbours is negligible (Roy *et al.* 1996). The lateral dimension of the flow structures was measured using two triplets of ECMs fixed on two wading rods positioned side by side (figure 3*b*). The three ECMs were separated on each wading rod by 8 cm with the lowest sensor being 12 cm above the river bed. Two arms, which could slide on a wooden beam set perpendicular to the flow, were used to hold the wading rods. One arm was gradually moved away from a fixed arm to obtain separation distances between each triplet of 7, 12, 17, 27, 37, 47, 57, 77, and 97 cm. The seventh ECM was at the centre between the two uppermost ECMs of each triplet. The average flow depth was 31 cm. At each separation distance, streamwise velocities were measured for five minutes. For each deployment, care was taken to avoid the presence of large protruding clasts and pebble clusters upstream from the sensors.

2.2. *Data validation*

Velocity time series were visually scrutinized to identify abnormal signals and conspicuous spikes. For the lateral and longitudinal deployments, velocities measured by one of the ECM had variances three to four times higher than those obtained from the other sensors. The data from this sensor were removed from further analysis because it was clearly out of range. During the lateral deployment, the velocity data measured from the ECMs located near the water surface had frequent spikes. Undulations of the water surface may have affected the response of the sensor as part of the sampling volume could have been out of the water for small portions of the time. Velocity records having spikes of that kind were truncated. Finally, power spectra of the velocity fluctuations were used to assess the quality of the time series

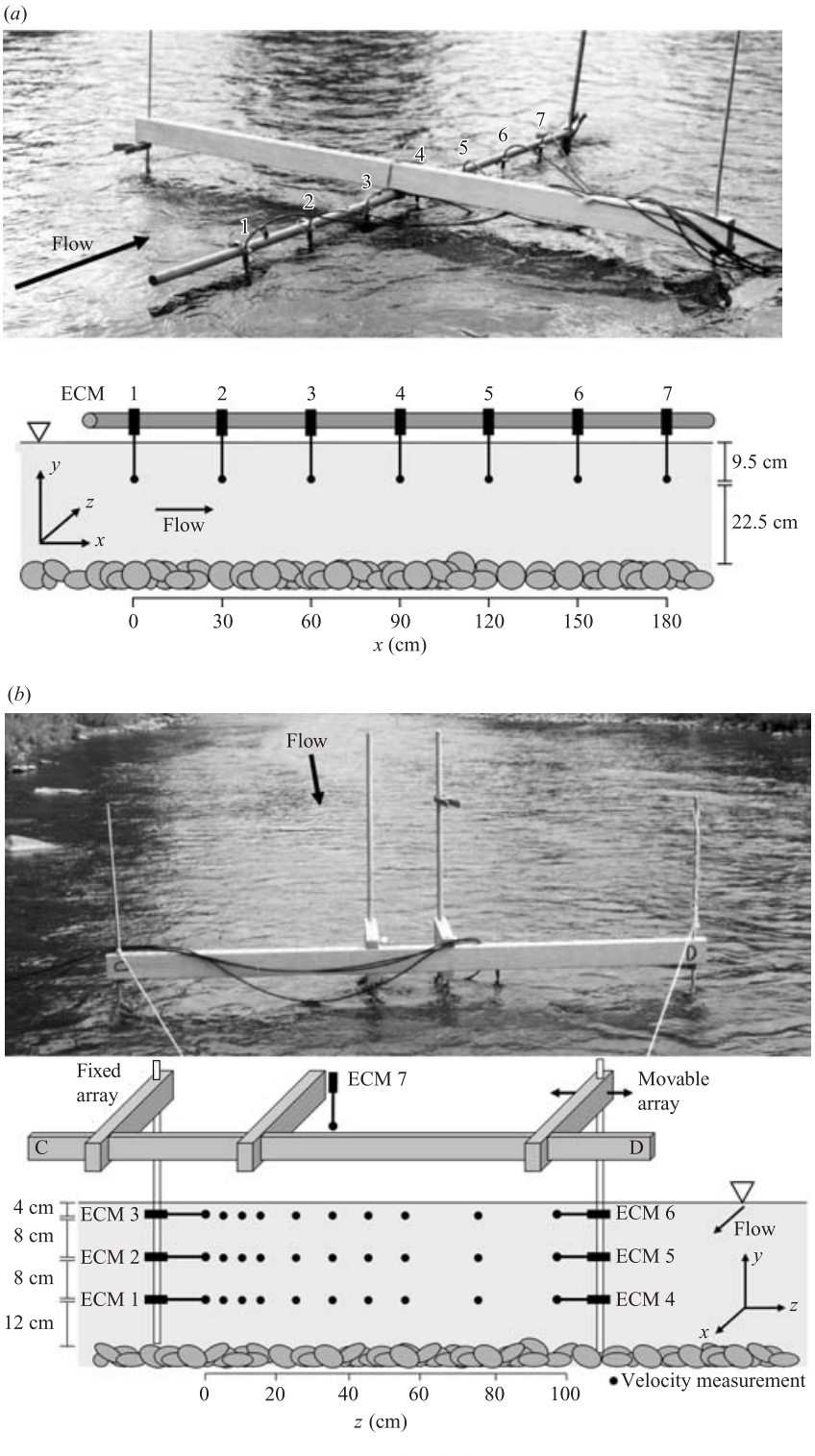

FIGURE 3. (*a*) Diagram showing the longitudinal deployment of the seven electromagnetic current meters. (*b*) Set-up to measure the lateral extent of coherent flow structures using an assemblage of seven ECMs.

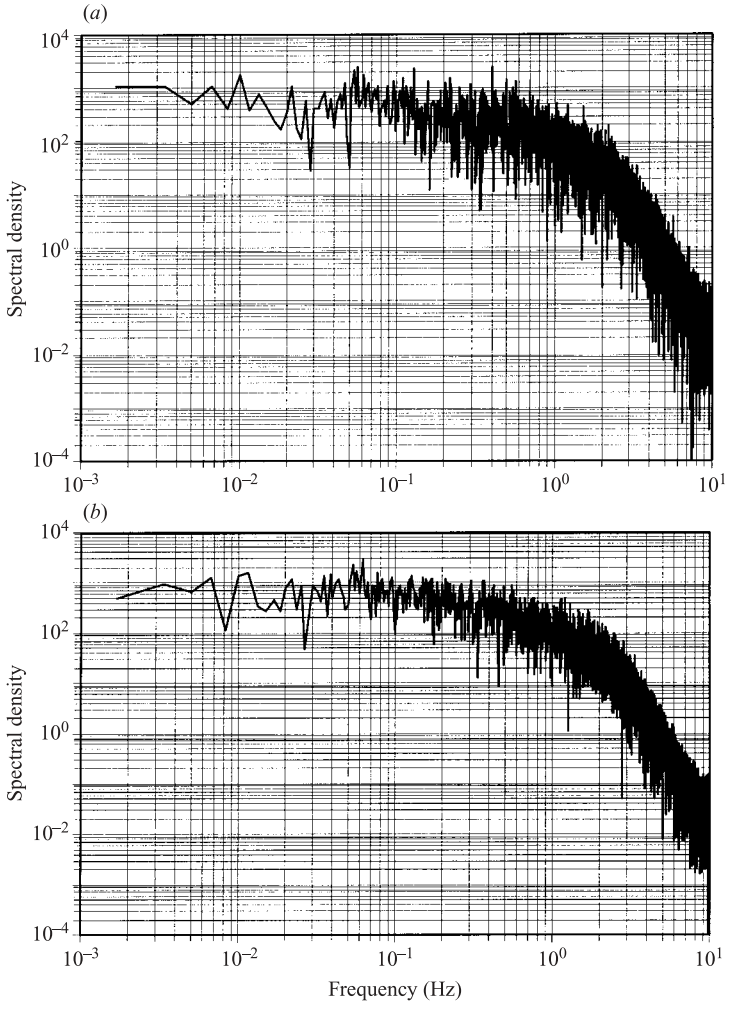

FIGURE 4. Power spectrum of the streamwise velocity component computed for (*a*) ECM 2 and (*b*) ECM 4. The data are from the longitudinal deployment (see figure 3*a* for the location of the sensors). Spectral densities represent average values computed from two non-overlapping series of 10 min extracted from the whole 20 min time series.

following the guidelines of Lapointe *et al.* (1996). Figure 4 presents power spectra computed for two ECMs for a period of ten minutes. The spectral densities represent average values based on a computation over two series of ten minutes for each sensor. The spectra show the expected –5/3 slope in the higher frequencies with a steeper roll-off in the higher frequencies caused by the R/C filter of the ECMs (Roy, Biron & Lapointe 1997). The spectra did not display any significant peak thus allowing us to conclude that the velocity signals were not affected by electronic noise (Lapointe *et al.* 1996).

To generate replicates and increase confidence in the statistical analyses, all velocity signals were split into one-minute time series. The use of one-minute samples is based on a study by Buffin-Bélanger (2001) who has shown that this record length yields robust statistics for turbulent flows above a gravel-bed river. Shorter time periods resulted in too much variability among the samples. This variability becomes stable

Study		Y (m)	U ($m\,s^{-1}$)	u^* ($m\,s^{-1}$)	$Re^{(1)}$ ($\times 10^3$)
Present study	Eaton Nord River, Can	0.28–0.67	0.36–0.67	0.005–0.013	200
Experimental channel					
Kirkgöz (1989)	Gravels	0.07–0.15	0.09–0.72	0.006–0.034	30
Grass *et al.* (1991)	Spheres	0.05	0.10–0.11	0.006–0.009	4
Ferro & Baiamonte (1992)	Coarse gravels	0.03–0.48	0.20–0.96[2]	0.026–0.067	100
Grass & Mansour-Tehrani (1996)	Spheres and gravels	0.05	0.11–0.23	0.006–0.016	7
Defina (1996)	Sperical gravels	0.01–0.10	0.11–0.60	0.018–0.051	10
Papanicolaou *et al.* (2001)	Spheres	0.05–0.08	0.25–0.88	0.031–0.093	30
Shvidchenko & Pender (2001)	Uniform gravels	0.03–0.10	0.38–0.98	–	30
Lawless & Robert (2001)	Gravels and pebbles	0.14–0.30	0.25–0.40	0.005–0.099	60
Gravel-bed river					
Bergeron & Abrahams (1992)	Swift River, USA	0.45–0.51[3]	0.90–1.16[3]	0.064–0.140	400
	Elton Creek, USA	0.42–0.49[3]	0.75–1.06[3]	0.040–0.245	300
	Cattaraugus, USA	0.43–0.50[3]	0.87–1.34[3]	0.063–0.237	400
	Rivière au Saumon, Can	0.33–0.40[3]	0.57–1.09[3]	0.063–0.169	200
Robert *et al.* (1992)	Eaton Nord River, Can	0.35	0.35–0.50[4]	0.035–0.085	100
Kirkbride & Ferguson (1995)	Beauty Creek, Can	0.55	0.6	–	300
Clifford (1996)	Langden Brook, UK	0.08–0.72	0.01–1.20[4]	–	200
Robert (1997)	Little Rouge River, Can	0.28–0.54	0.43–0.97	0.029–0.066	200
Nikora & Smart (1997)	Ashburton River, NZ	0.16–0.64	0.86–1.50	0.112–0.451	400
	Waiho River, NZ	0.30–1.15	0.76–2.06	0.093–0.856	800
	Hurunui River, NZ	0.56–1.81	1.77–3.12	0.152–0.245	2 000
Smart (1999)	Rangitata River, NZ	0.30–2.20	0.89–3.04	0.20–1.45	2 000
Dinehart (1999)	North Fork Trout River, USA	0.82–2.20	1.10–3.40	–	3 000
Buffin-Bélanger *et al.* (2000*a*)	Eaton Nord River, Can	0.35–0.40	0.34–0.41	0.024–0.396[3]	100

[1] Values estimated from mid-range Y and U and v at 10 °C. [2] Estimated from discharge.
[3] Personal communication. [4] Estimated from figures.

TABLE 2. Characteristics of the flow in this study compared to those of flows studied in experimental channels and gravel-bed rivers.

at a record length of one minute. With the chosen sampling frequency and duration the variance losses in the streamwise velocity signals are also minimal. Using the diagrams provided by Soulsby (1980), we have estimated that the loss of variance in the signals is less than 10%. The variance is lost mostly in the high frequencies.

The characteristics of the flow in this study fall well within the range of flows used in previous studies both in experimental channels and in gravel-bed rivers (table 2). Average flow characteristics are shown in figure 5 for the five velocity profiles sampled in the vertical deployment. The profiles exhibit some variability but they appear to

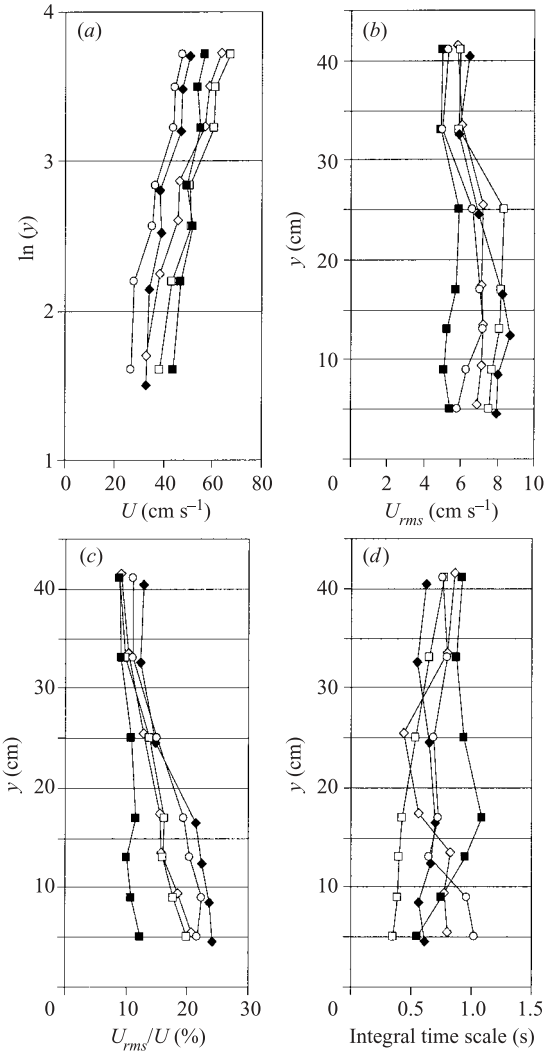

FIGURE 5. Turbulence statistics for the streamwise velocity component at seven points measured simultaneously on a vertical profile: (*a*) average velocity (U), (*b*) standard deviation (U_{rms}), (*c*) turbulent intensity (U_{rms}/U), and (*d*) integral time scale. The results from five 2 min series are shown and each symbol corresponds to an individual profile. The flow depth ranges from 46 to 59 cm.

be typical of those obtained over rough beds in flume studies (Kirkgöz 1989; Grass *et al.* 1991; Krogstad, Antonia & Brown 1992; Ferro & Baiamonte 1992; Lawless & Robert 2001; Papanicolaou *et al.* 2001) and in gravel-bed rivers (Robert *et al.* 1992; Roy *et al.* 1996; Clifford 1996; Nikora & Smart 1997; Buffin-Bélanger & Roy 1998; Smart 1999). Streamwise velocity follows a logarithmic profile over the entire water column (figure 5*a*) whereas the standard deviation and turbulence intensity, as expressed by U_{rms}/U, are higher in the near-bed region (figure 5*b*, *c*). The integral time scale (figure 5*d*) estimated from the autocorrelation function is nearly constant throughout the water column with an average value of 0.70 s. This is similar to the value of 0.65 s reported by Roy *et al.* (1996) in a similar environment. Figure 6 shows

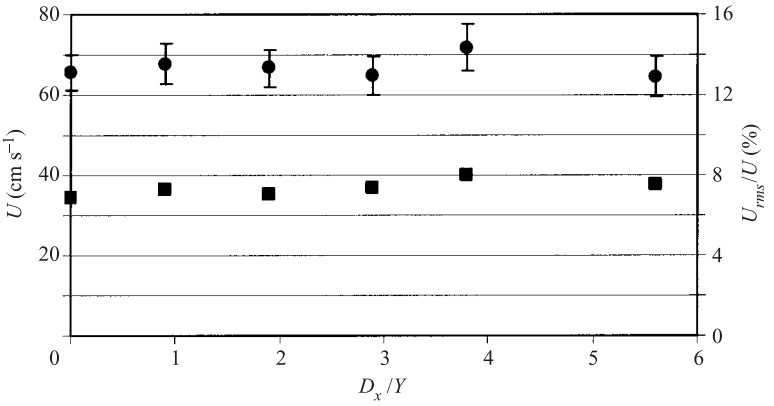

FIGURE 6. Londitudinal distribution of the average streamwise velocity (black circles) and of turbulence intensity (black squares). The velocity measurements are obtained from six electromagnetic current meters deployed at the same height (9.5 cm) below the water surface. The flow depth is 32 cm.

the averages and turbulence intensity (U_{rms}/U) of the streamwise velocity component measured at each position in the longitudinal deployment. There is little variability among the sensors. Average flow velocity is 66 cm s^{-1} and the turbulence intensity is similar for all sensors with an average value of 8%, a value that is slightly lower than the average of 13% observed at a similar height in the vertical profile (figure 5). This discrepancy may be due to the variability in bed roughness.

2.3. *Data analysis*

In order to ascertain the properties of large-scale turbulent flow structures we have focused on four variables: duration (D), frequency (F), length (L), and advecting velocity (V_a). The length (L) is estimated from Taylor's hypothesis on frozen turbulence in which durations are converted into distances. This hypothesis may not apply in flows where a single large-scale flow structure can undergo rapid evolution or interaction with neighbouring structures (Zaman & Hussain 1981). As will be shown later, the longitudinal deployment of the ECMs reveals that the large-scale flow structures investigated here conserve their coherence over a significant distance (up to six times the flow depth). This might not be true, however, in the near-bed region where turbulence is more intense. Using DNS and LES of turbulent channel flow as well as measurements in a turbulent boundary layer, Piomelli, Ballint & Wallace (1989) concluded that Taylor's hypothesis remains valid above the buffer layer. Hence, given the relatively low values of turbulence intensity of the flow measured here and the spatial persistence of the flow structures, it seems reasonable to use Taylor's hypothesis for most of the measurement points except in the near-bed region. From cross-correlation functions between time series sampled by two acoustic Doppler velocimeters, Nikora & Goring (2000) have shown that Tailor's hypothesis is applicable for the 90% of the upper section of a flow above a gravel-bed.

The advecting velocity (V_a) is determined only for the longitudinal deployment of the ECMs. It can be estimated from

$$V_a = \frac{D_{ECMa-ECMb}}{T_{ECMa-ECMb}} \tag{1}$$

where $D_{ECMa-ECMb}$ is the distance between two sensors and $T_{ECMa-ECMb}$ is the time

taken by the flow structure to cover that distance. Due to the fact that flow structures evolve over time and space, it is challenging to determine the time taken by an individual structure to travel the distance between two sensors. Experimental studies have shown that the survival distance of flow structures can be relatively long compared to the boundary layer thickness (Favre *et al.* 1957; Brown & Thomas 1977; Krogstad, Kapersen & Rimestad 1998) and flow depth (Dinehart 1999; Nikora & Goring 2000).

The four variables are extracted from the simultaneous velocity signals using three types of analysis: space–time velocity matrices, space–time correlation and conditional sampling. Space–time velocity matrices are a simple but informative tool to picture the instantaneous velocity signals measured simultaneously at several points in the flow. This type of visualization was first used in gravel-bed rivers by Buffin-Bélanger *et al.* (2000*a*) to represent the vertical extent of flow structures. In the matrices, the vertical and longitudinal axes correspond to the distance between sensors and to the duration of the sampling period, respectively. Each cell represents a standardized velocity fluctuation and is coloured according to its deviation from the average velocity at the sensor location. Here, red and blue cells are velocity fluctuations that are higher and lower than the average velocity, respectively. Space–time velocity matrices depict the structure of the flow field from which the size and scale of individual flow structures as well as their advecting velocity can be estimated.

Space–time correlation analyses (STCA) were performed for several combinations of separation distances between two sensors. This technique is based on the estimation of correlation values between two simultaneous velocity signals sampled at different locations in space and for different time lags (Favre *et al.* 1957; Brown & Thomas 1977; Nakagawa & Nezu 1981; Robert, Roy & De Serres 1993). In the analysis, we have considered two quantities derived from STCA: the maximum correlation value and the time lag where this maximum occurs (Buffin-Bélanger *et al.* 2000*a*). The correlation coefficient is computed from

$$c_{u_1-u_2}(d) = \sum_{t=1}^{N-d} (u_{1t} - \langle u_1 \rangle)(u_{2t+d} - \langle u_2 \rangle) \qquad \text{for } d \geqslant 0, \tag{2}$$

$$c_{u_1-u_2}(d) = \sum_{t=1-d}^{N} (u_{1t} - \langle u_1 \rangle)(u_{2t+d} - \langle u_2 \rangle) \qquad \text{for } d < 0 \tag{3}$$

and

$$r_{u1-u2}(d) = \frac{c_{u1-u2}(d)}{s_{u1} s_{u2}} \tag{4}$$

where u_t, $\langle u \rangle$, s_u and N are respectively an instantaneous velocity, the average velocity, the standard deviation and the number of elements in the velocity times series u_1 and u_2; d, a temporal lag; and c_{u1-u2}, the covariance between the times series u_1 and u_2. The confidence interval for the STCA performed on velocity time series has to take into account the presence of significant autocorrelation within the signal. The observed autocorrelation function of a velocity signal reflects the combined effect of the filter of the ECM, in this case a RC filter, and of coherence of the turbulent flow structures. Even in the absence of autocorrelation between flow velocities measured at different times, the RC filter does introduce a correlation that is statistically significant at least for the 4 or 5 first time lags (Roy *et al.* 1997). In the presence of a strong autocorrelation in the streamwise velocity signal, this effect could be neglected. In this paper, we have used the permutation procedure presented by

Buffin-Bélanger *et al.* (2001) to estimate confidence intervals under the conditions of significant autocorrelation within the velocity signal. This technique relies on the calculation of space–time correlations between several velocity signals that have not been sampled at the same time. This represents the null hypothesis of no correlation between the signals and gives the distribution of possible correlation values given the autocorrelation within the signals. The distribution of the correlation coefficients is used to determine the standard error from which confidence intervals are then estimated.

Because space–time correlation analyses do not describe the dynamics of individual coherent structures (Nezu & Nakagawa 1993), conditional sampling was applied to velocity signals in order to detect and quantify individual flow structures. Several techniques have been developed to detect turbulent flow structures in velocity time series (Bogard & Tiederman 1986). Using data collected in an environment that is similar to the one studied here, Roy *et al.* (1996) have shown that most techniques yield similar results. Here, we use two different techniques that rely on the sampling of one velocity component: the U-Level detection technique as modified by Luchik & Tiederman (1987) and a modified version of the WAG detection scheme initially introduced by Antonia, Bisset & Browne (1990). The U-Level detection technique is used to document events with a velocity signature that is higher or lower than the average velocity plus or minus a fraction of the standard deviation of the velocity distribution. The modified U-Level uses a different threshold value for the beginning and the end of the event. This minimizes the detection of several events that are in fact part of the same flow structure. The modified U-Level technique begins the detection of an event when

$$|u'| > ks_u \tag{5}$$

and ends the detection when

$$|u'| < pks_u \tag{6}$$

where u' is the velocity fluctuation; k, a threshold value; s_u, the standard deviation of the velocity time series; and p takes a value between 0 and 1. The U-level detection scheme has been applied using threshold values of $k = 0$, 0.65, and 1.3 with $p = 0.25$. Bogard & Tiederman (1986) have shown that $k = 1.3$ gives results that are similar to those obtained from flow visualization experiments in a laboratory flume. A probability p of 0.25 was suggested by Luchik & Tiederman (1987) and has been used since by several authors (i.e. Shah & Antonia 1989; Krogstad *et al.* 1992). The WAG detection scheme was developed to look for large-scale turbulent events from the presence of rapid transitions in the velocity signal (Antonia *et al.* 1990; Krogstad *et al.* 1998). It picks out the shear layer between successive high- and low-speed events. In the WAG scheme, a detection occurs when

$$|\langle\beta\rangle_w| > ls_u \tag{7}$$

where β is a measure of the local velocity gradient; w, a time window for which the velocity gradient is calculated; l, a threshold value; and s_u, the standard deviation for the entire velocity time series. Here, the slope β is computed from the linear least-square regression equation between velocity and time within the detection window. The WAG technique will be used mainly to determine the advecting velocity. Because the sensitivity of the advecting velocity to the choice of w and l has been found to be very low (Krogstad *et al.* 1998), values of $w = 1.0$ s and $l = 0.5$ were chosen, consistent with values used in previous studies.

In order to estimate the advecting velocity of individual events, conditional sampling techniques are also used to track the large-scale coherent events in the streamwise direction at the different positions where the sensors were deployed. Because flow structures evolve and interact over space and time, it is difficult to make sure that a structure is detected again at a further location downstream (Blackwelder 1977). It is also assumed that the flow structure travels in the direction of the sensor array. Here, the procedure adopted was first to identify an event as it occurs at the sensor of the upstream location using either the modified U-Level or the modified WAG detection techniques. Because we were interested in the larger-scale flow structures, we have considered only events lasting more than 1 s. The velocity time series of a detected event were correlated in turn with the velocity signals of similar length and for several time steps from each sensor located downstream. The time delays between peaks of correlation at the different sensors were used to construct a frequency distribution of the delays from which a significant peak value can be extracted (Krogstad *et al.* 1998).

3. Results

3.1. *Space–time velocity matrices*

Figure 7 presents two space–time matrices of the streamwise velocity component from the vertical deployment of the ECMs. Clear regions of high (red) and low (blue) flow regions that tend to occupy a large portion of the water column can be seen on both matrices. These interlaced regions of fast and slow moving fluid emerge as dominant features for all the space–time matrices that were produced. Visual inspection reveals that the duration of the high- and low-velocity flow regions generally varies from 1 to 5 s. Given the average flow depth (47 cm) and velocity (46 cm s^{-1}), the length of the flow structures is estimated to be between one and five times the flow depth. The frequency (F) of the large-scale structures of each type is between 0.07 to 0.12 Hz. The high- and low-velocity flow regions tend to be tilted obliquely towards the downstream end with the top portion of the flow structure being ahead of the bottom portion (see figure 7*a* between 20 and 40 s). A similar pattern of large-scale fast and slow moving structures has been reported by Grass (1971) and Grass *et al.* (1991).

In figure 8, a space–time velocity matrix of the streamwise velocity component is shown for the longitudinal configuration for a 1 min time series. The velocity matrix is well structured as clear oblique regions of low (blue) and high (red) velocity are apparent. Similar patterns were observed in all 1 min time series. Generally, these high- and low-velocity flow regions seem to last between 1 and 3 s and appear to persist over the entire distance of sampling (180 cm). Taking into account the average velocity and depth of the flow (67 cm s^{-1} and 32 cm respectively), the structures depicted here have length of two to six times the flow depth and persist over a distance of 5.6 times the flow depth. Between 5 and 8 regions of low and high velocity are observed in the matrix (figure 8*a*). This gives a frequency (F) ranging between 0.08 and 0.13 Hz.

An inspection of the details of the matrix reveals that the general pattern often becomes complicated and variable. Two examples of such changes in the pattern are related to the advection of low-velocity regions (figure 8*b*). The low-velocity region observed at 50 s seems to increase its advecting velocity as the time it takes to flow the first 60 cm appears to be longer than the time taken to flow the last 60 cm. The other low-velocity region at 55 s seems to conserve its advecting velocity but its duration seems to decrease as it flows downstream, passing from 3 s duration to less than 2 s duration. This illustrates visually the dynamics and interactions between the large-scale structures that are present in figure 7.

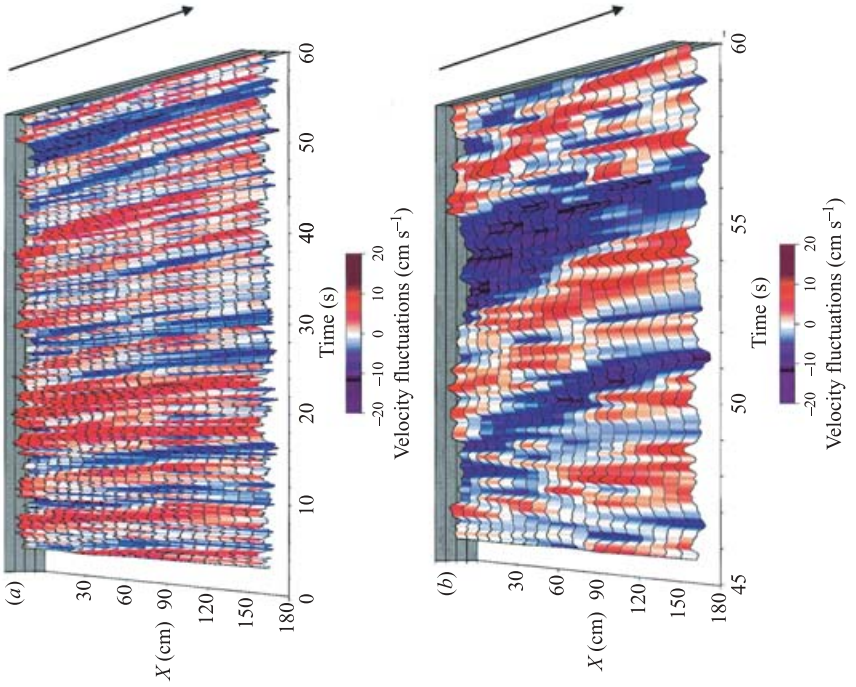

FIGURE 8. For caption see facing page.

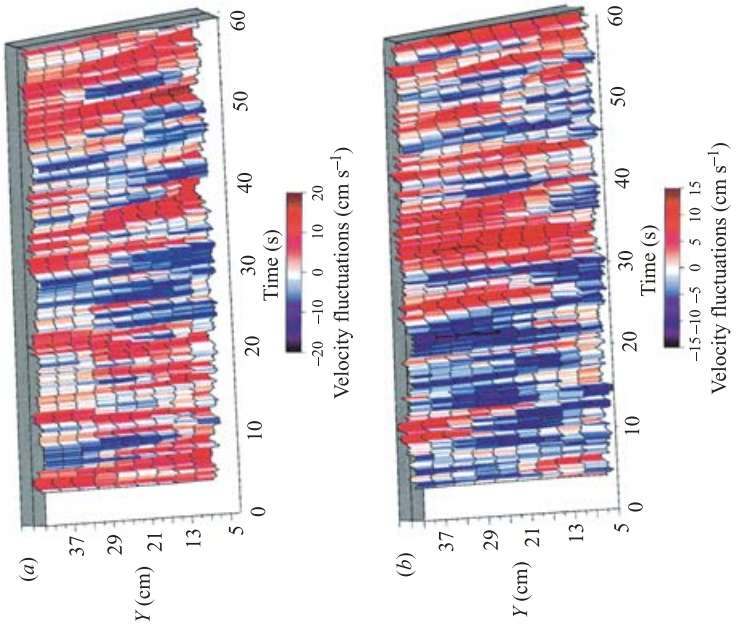

FIGURE 7. For caption see facing page.

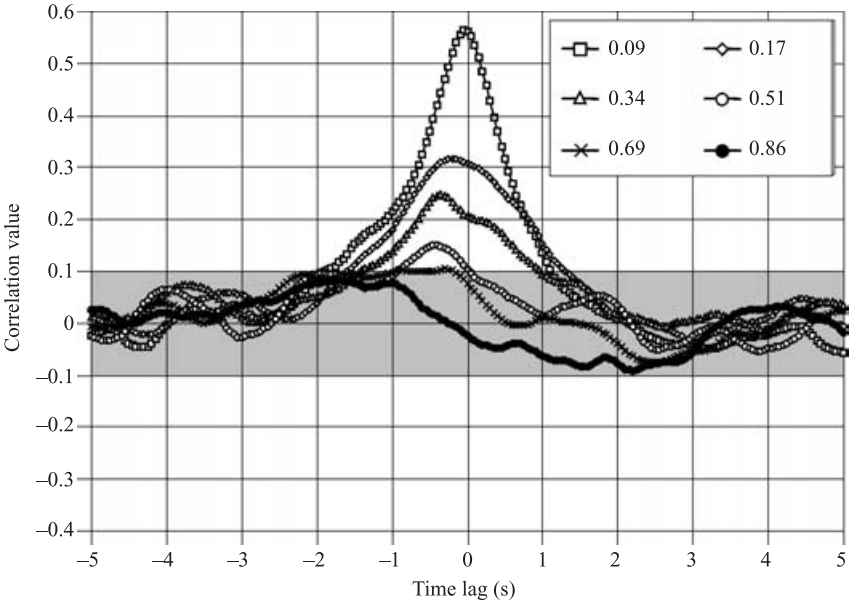

FIGURE 9. Space–time correlation analysis of the streamwise velocity component from the vertical deployment of seven ECMs. Each line includes all possible combinations of two ECMs with the same separation distance between the sensors. The values of separation distances shown in the legend are normalized by the depth of flow.

3.2. *Space–time correlation analysis*

Space–time correlation analyses were performed for all possible combinations of pairs of the seven ECMs for the five vertical velocity profiles. Figure 9 shows that the maximum correlation value decreases as the vertical distance between the sensors increases. Considering the distances covered in this experiment, all maximum values appear to be significant at a significance level of 0.05. Also, the lag at which the maximum correlation occurs increases with the vertical distance between the sensors. Here, a negative lag means that velocity fluctuations measured by a near-bed sensor are correlated with the velocity fluctuations measured by a near-surface sensor at an earlier time. This suggests the presence of coherent flow structures occupying the entire depth of the flow and having an oblique front inclined in the flow direction as already observed on the space–time velocity matrices.

The angle of propagation of the large-scale flow structures can be assessed from the temporal lag at which the maximum correlation occurs between each pair of sensors deployed vertically (Buffin-Bélanger *et al.* 2000*a*). Here, we have estimated an average angle of 25° from 21 combinations of two sensors for each vertical profile. This

---

FIGURE 7. Two examples of tridimensional space–time matrices for the streamwise velocity fluctuations measured on a vertical profile by seven ECMs. The time series are 60 s long in both cases. Velocity fluctuations were interpolated in between the locations of the sensors. Flow depth and average velocity were 47 cm and 46 cm s^{-1}, respectively.

FIGURE 8. (*a*) A longitudinal space–time matrix for the streamwise velocity fluctuations based on six ECMs. The time series is 60 s long. Velocities were interpolated in between velocity sensors. (*b*) Zoom of the last 15 s of the matrix shown in (*a*).

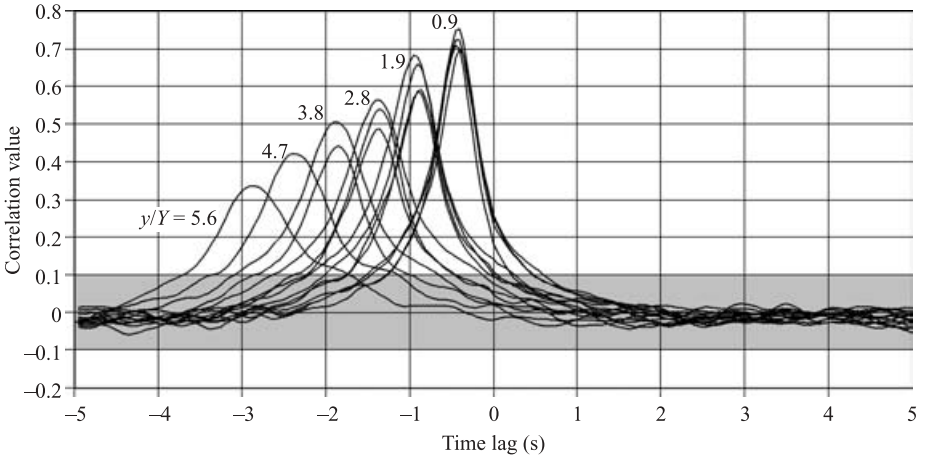

FIGURE 10. Space–time correlation analysis for the streamwise velocity component measured in the longitudinal deployment of the array of ECMs. All the possible combinations of two ECMs are plotted. Separation distances indicated by the side of the curves are normalized by the depth of flow.

means that the typical structure is inclined, from a line normal to the bed, towards the downstream direction. There was, however, a broad range of values, some of which were negative. There exists no vertical trend in the value of the angles. This result contrasts with previous measurements made by Buffin-Bélanger *et al.* (2000*a*) who have reported an average angle of 36° and a decreasing trend of the angles towards the surface. The lower average angle may be caused by the presence of infrequent but very high negative angles. However, with less than 15% of the angles being negative, it seemed clear that the advecting large-scale flow structures are generally inclined in the flow direction.

Two other features on figure 9 are of interest. Firstly, the interval of time over which the correlation coefficient is significantly different from zero ranges between 1 s, for the longest distance between two sensors, and 3 s, for the shortest distance between two sensors. This period is related to the temporal coherence of the structures. Using Taylor's hypothesis and given that water depth varies between 46 and 59 cm and average velocity is 45 cm s^{-1}, this diagram suggests that the length of the flow structures lies between one and three times the depth of flow. Secondly, it appears that a significant negative correlation value is observed at a time lag of 2 s for the combination involving the two sensors having the greatest separation distance in the vertical. Here, the negative correlation implies that an increasing velocity at the bed is matched with a decreasing velocity at the highest region in the flow, and *vice versa.* This again suggests the overhanging shape of the average flow structure.

Figure 10 presents cross-correlation analyses for all possible separation distances between the ECMs for the longitudinal deployment. The maximum correlation value decreases at a constant rate with the distance between the probes and remains significantly different from 0 ($\alpha = 0.05$) for all normalized distances. This implies that the flow structures persist over a distance of 5 to 6 times the water depth. At a lag of zero, correlation values decrease with increasing distance between the sensors and become non-significant at a distance between 1.9 and 2.8. A similar pattern has been documented by Roy *et al.* (1996) who studied the space–time correlation at two heights above a gravel-bed river and their data fit well with the observations reported

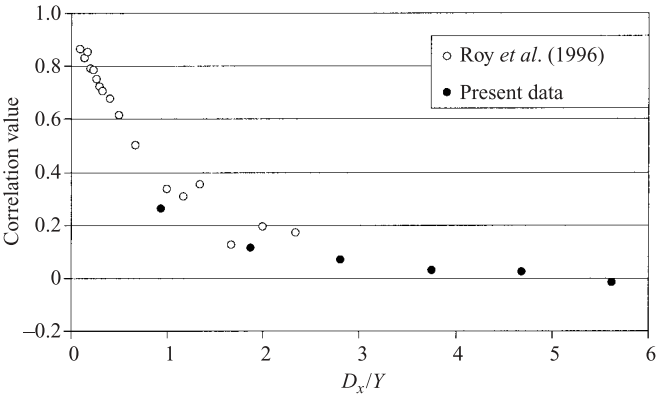

FIGURE 11. Correlation values obtained at a lag of zero in figure 10. Results from Roy *et al.* (1996) obtained in a gravel-bed river using shorter separation distances between the sensors are superimposed on the results obtained in this study. Flow depth (30 cm vs 32 cm), average flow velocity (61 cm s^{-1} vs 67 cm s^{-1}) and height of the sensors above the bed (21 cm vs 22.5 cm) were nearly identical in both studies. Sampling frequency in the data from Roy *et al.* (1996) is 10 Hz.

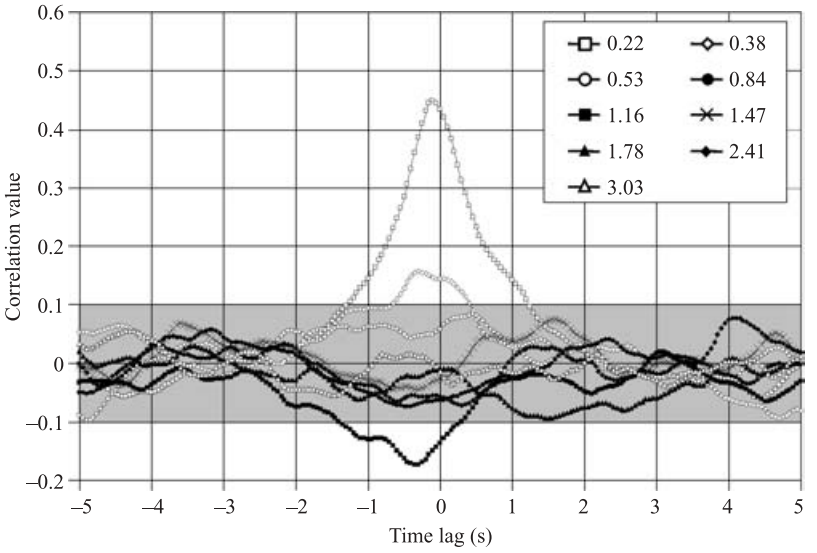

FIGURE 12. Space–time correlation analysis for streamwise velocity component obtained in the lateral deployment of the array of ECMs. Separation distances shown in the legend are normalized by the flow depth.

here (figure 11). From Taylor's substitution, this suggests that the average length of the flow structure is close to twice the flow depth. Finally, the advecting velocity is given by the lag at which maximum correlation values occur. On average, maximum correlation values between a separation distance of 30 cm occur at a time lag of 0.48 s. This corresponds to an advecting velocity of 62 cm s^{-1} for the average flow structure. This velocity is close to the average velocity of 66 cm s^{-1} measured by the ECMs.

Figure 12 shows the results for the STCA computed between the two pairs of ECMs deployed laterally. Maximum correlation decreases rapidly with distance and

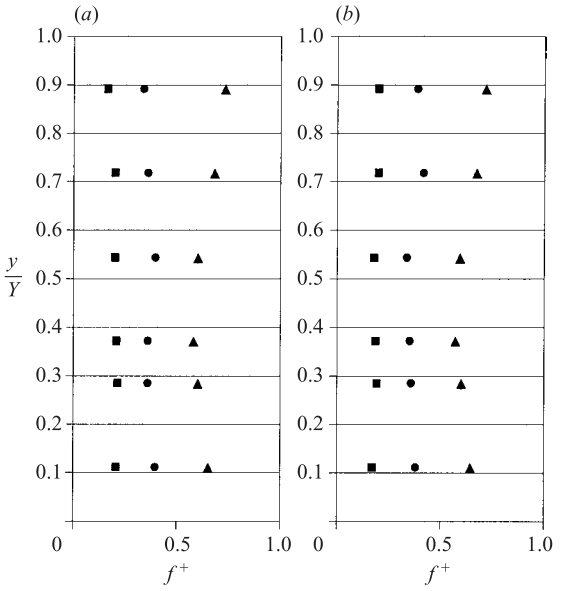

FIGURE 13. Temporal frequency of (*a*) low- and (*b*) high-speed flow events detected using the modified U-level scheme applied to the velocities measured on the vertical profile with seven ECMs. Three different threshold values for the detection are used (triangle $k = 0$; circle $k = 0.65$; and square $k = 1.3$).

at a normalized distance of 0.53 it is no longer significantly different from zero ($\alpha = 0.05$). At almost twice this distance (normalized distance of 1.16), the maximum correlation value becomes significant again but with a negative sign. This suggests that high-speed flow regions are found side-by-side with low-speed flow regions at a normalized distance of 1.16. A consequence of this proximity between the large-scale flow structures is that energy dissipation may be dominated by the transverse cross-stream shear. Our evidence is not yet sufficient to confirm this idea.

3.3. *Conditional sampling of individual events*

Figure 13 shows the frequencies of high- and low-speed flow structures detected by the modified U-level scheme for the data obtained from the vertical deployment. These values are in agreement with previous results obtained from various detection schemes (Roy *et al.* 1996). However, they are higher than the frequency determined by the visual inspection of the velocity matrices. This discrepancy is due to the detection of small events by the U-level scheme at all threshold values. Figure 14 shows the frequency distribution of duration for the low-speed events using the thresholds of $k = 0$ and $k = 1.3$. It is clear that short-duration events will tend to pass undetected by a visual examination of the velocity matrix. If one takes into account only an event lasting more than 1 s, the frequency then decreases significantly. For the vertical deployment, such a calculation yields mean frequency values of 0.13 Hz, 0.08 Hz and 0.04 Hz for detection using $k = 0$, 0.65, and 1.3 respectively. These frequencies are closer to the one observed for the space–time velocity matrices. Secondly, the frequency of events appears to be constant throughout the water column for a given threshold value (figure 13). This observation is also consistent with previous studies (Roy *et al.* 1996) and is particularly clear for $k = 1.3$. For $k = 0.65$ and $k = 0$, there is a tendency for event frequency to decrease from the bed towards the centre of the

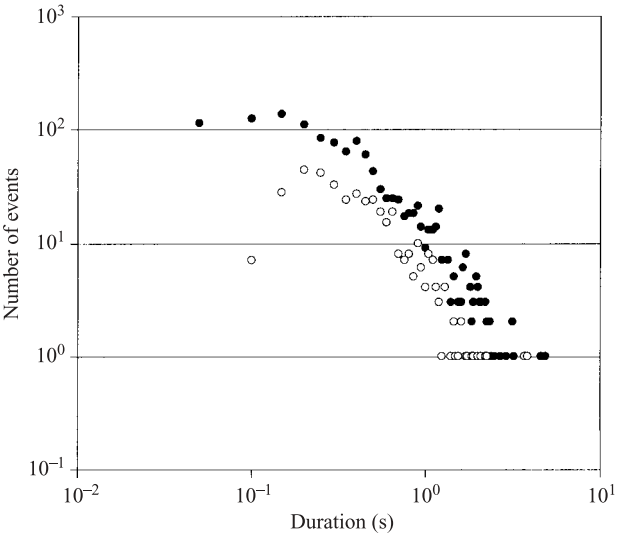

FIGURE 14. Examples of the frequency distribution of the duration of bursting events detected by the U-level scheme for two threshold values (black circle $k=0$; white circle $k=1.3$).

water column before it increases slightly towards the water surface. As the detection of coherent structures is prone to errors, it is difficult to know if these trends are significant.

Conditional sampling techniques were used to detect the coherent flow structures that could then be tracked from the upstream to the downstream sensor in the longitudinal deployment. The frequency distribution of the time delays at which the maximum correlation value occurs between the combination of sensors are shown on figure 15 for all events detected using the modified U-Level and a threshold value $k=0$. As expected, the time delay at which the maximum correlation is occurring increases with the separation distance between the sensors. At higher separation distances, it becomes difficult to identify a dominant time lag at which the maximum correlations are recorded.

We used the mode of the frequency distributions to represent the time taken on average by the flow structures to travel the distance between the two sensors. In the present case, a clear mode appears for all distributions except for the last two separation distances (150 and 180 cm). The peak at which maximum correlation occurs can be used to estimate an average advecting velocity (Krogstad *et al.* 1998). The modes were extracted from the distributions obtained from the modified U-level, with $k=0$ and $k=1.6$, and from the modified WAG detection schemes. Table 3 summarizes the results and presents the estimated advecting velocities using the first four separation distances. From our results, it appears that the advecting velocity of the high-velocity regions is 10% higher than the advecting velocity of the low-velocity regions (9% and 11% for $k=0$ and $k=1.3$, respectively). These results compare well with the 15% and the less than 20% obtained by Guezennec, Piomelli & Kim (1989) and Krogstad *et al.* (1998) using similar detection schemes but different velocity measurement techniques. In natural rivers, Dinehart (1999) and Nikora & Goring (2000) have estimated an eddy convection velocity for the whole of the flow that was comparable with the local mean velocity. Using schemes that can detect turbulent events, it is possible to assess the convection velocity for different types of flow

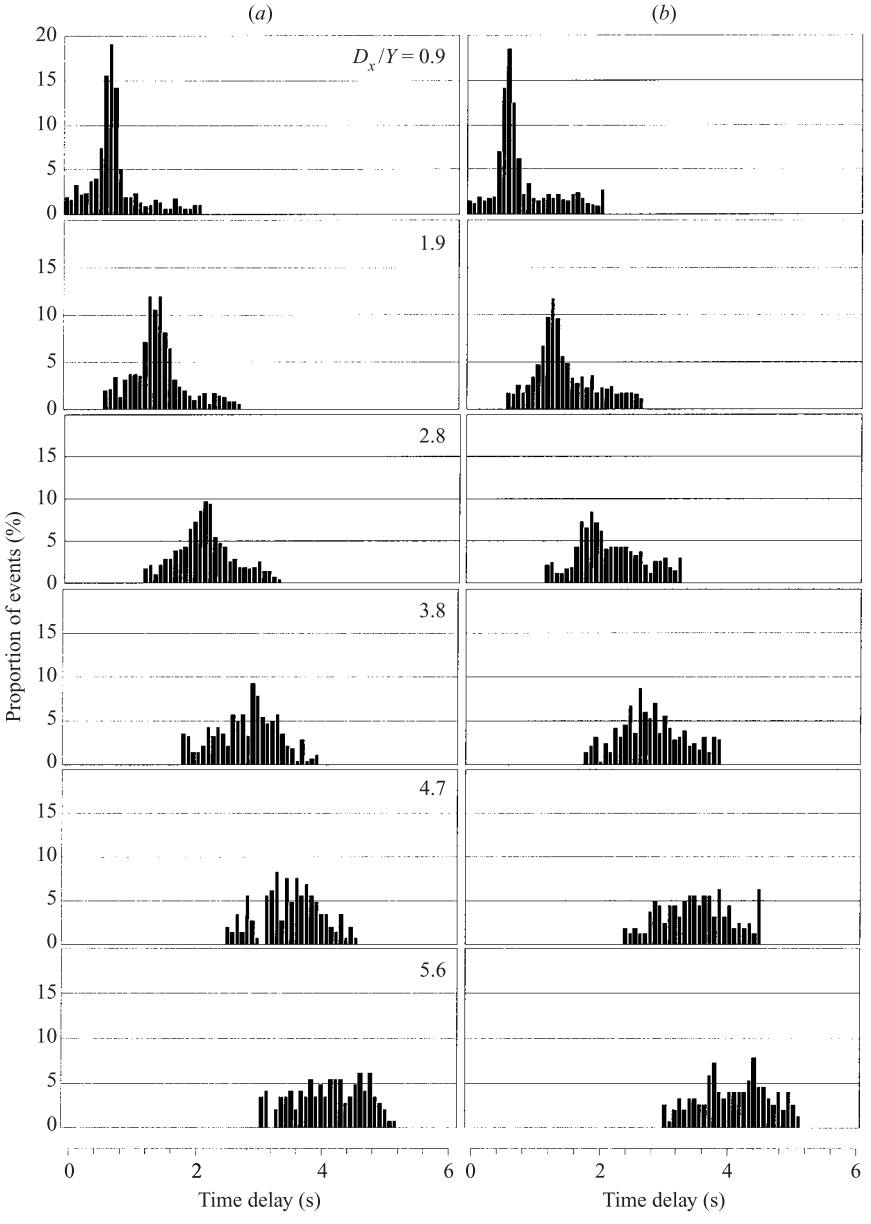

FIGURE 15. Probability density function of the maximum correlation coefficients between the conditional sampling signature of (*a*) a low- or (*b*) high-speed event detected at an upstream sensor and the velocity time series during a time window with the same length measured at a sensor located downstream.

structures. The WAG scheme allows detection of rapid transitions in the velocity signal, which correspond to shear zones between high- and low-velocity regions. The results show that there is no significant difference between the advecting velocities for the negative discontinuities and for the positive discontinuities. Both types of structures are advecting downstream at a velocity that lies in between the advecting velocities of the high- and low-velocity regions detected with the U-level technique.

		High-speed flow structures			Low-speed flow structures		
	S	N	Lag	V	N	Lag	V
(*a*)	30	581	0.45	66.7	585	0.50	60.0
	60	623	0.85	70.6	600	0.90	66.7
	90	469	1.30	69.2	454	1.45	62.1
	120	317	1.80	66.7	310	1.95	61.5
	150	179	2.45	61.2	160	2.20	68.2
	180	179	2.95	61.0	160	2.80	64.3
Average (for $S = 30$ to 120)				68.3			62.6
(*b*)	30	170	0.45	66.7	181	0.50	60.0
	60	207	0.95	63.2	200	1.05	57.1
	90	164	1.38	65.2	151	1.55	58.1
	120	120	1.80	66.7	113	2.00	60.0
	150	76	2.45	61.2	64	2.35	63.8
	180	76	2.95	61.0	64	2.95	61.0
Average (for $S = 30$ to 120)				65.5			58.8
(*c*)	30	465	0.50	60.0	494	0.45	66.7
	60	462	0.90	66.7	504	0.95	63.2
	90	346	1.35	66.7	386	1.45	62.1
	120	230	1.85	64.9	260	1.85	64.9
	150	122	2.40	62.5	136	2.30	65.2
	180	122	3.10	58.1	136	2.85	63.2
Average (for $S = 30$ to 120)				64.5			64.2

TABLE 3. Advecting velocities of turbulent flow structures detected using U-level with two threshold values ((*a*) $k = 0$ and (*b*) $k = 1.3$) and (*c*) WAG schemes applied to the streamwise velocities measured through the longitudinal deployment of an array of six ECMs. (S: Separation distance between the sensors in cm; N: Number of structures detected; Lag: time lag at which correlation is maximized; V: advecting velocity of the structures in cm s^{-1}).

	Velocity matrices	Correlation analysis
Height	Y (v)	Y (v)
Length	(1–5) Y (v) (2–6) Y (L) (2–10) Y (l)	2–3 (v) 2–3 (L)
Width	0.5Y (l)	0.5–1 (l)
Spatial persistance	>5.6Y (L)	>5.6Y (L)

TABLE 4. Summary of dimensions (expressed as a function of flow depth, Y) of the large-scale turbulent flow structures described in this study. The dimensions are obtained from two techniques applied to the velocity measurements collected in the vertical (v), longitudinal (L) and lateral (l) deployments used in this study.

4. Discussion and conclusion

This study has confirmed the presence of large-scale flow structures in gravel-bed rivers. It has shown that these structures definitely scale with the outer flow variable, most importantly with the depth of flow (Y). Table 4 presents the scalings of the structures estimated from the space–time matrices and from space–time correlation analyses. A comparative scaling of y^+ for the vertical extent of the structures would

be in the order of 3000 to 4000, a value that is too large to suggest that the inner flow variables are relevant in the dynamics of these structures. The large-scale turbulent flow structures take the form of high- and low-speed wedges that occupy the entire depth of the flow and that are narrow and elongated. Given the extremely rough nature of the bed over which the water is flowing, it is quite astonishing that the scaling values presented herein are similar to those obtained from experiments in the laboratory, even those on smooth beds (table 1). These findings would support the notion that universal characteristics of the turbulent flow structures may exist in wall shearing flows (Grass *et al.* 1991; Grass & Mansour-Tehrani 1996).

The high- and low-speed flow wedges appear to flow side-by-side in a way that is consistent with Yalin's view of the pattern of alternating high- and low-velocity flow regions corresponding to a chessboard (Yalin 1992). A similar pattern of large-scale fast and slow moving structures has also been reported by Grass (1971) and Grass *et al.* (1991) who suggested, from flow visualization above homogeneous rough beds, that this pattern was related to the presence of horseshoe vortices created by shear layers lifted towards the surface. These vortical structures may be responsible for the boils observed by Jackson (1976) at the surface of river flows. Recently, other models have been proposed to account for the evolution of flow structures in the turbulent boundary layer and which could explain the size, shape and dynamics of the turbulent flow features observed in our data. From visual experimentation, Kaftori, Hetsroni & Banerjee (1994) have presented the funnel-shape vortex to describe the downstream advection of high- and low-speed flow regions. The funnel-shape vortex is mainly associated with the inner region of the flow. However, as seen in their conceptual model (see figure 31 in Kaftori *et al.* 1994), regions of high and low velocity connected with each other in the funnel shape are adjacent to one another. Schvidchenko & Pender (2001) have also presented a model based on a Lagrangian flow visualization realized in an experimental channel. In their model, the flow consists of an ordered sequence of long-lived three-dimensional large-scale eddies. These eddies carry alternate regions of high and low velocities and present scales that are well within the range obtained in the present study (tables 1 and 4).

Although we have obtained good estimates of the scaling values that describe the size of the large-scale flow structures in gravel-bed rivers, it remains difficult to describe the complex dynamics of these structures as they develop and advect downstream on a bed of such great complexity. For example, the quantitative data did not allow us to investigate the momentum exchange associated with the structures nor to examine satisfactorily the presence of smaller scale eddies that may play a key role in the development of the large-scale flow structures. Furthermore, we have little direct evidence on the dynamics of the near-bed region where ejections of low-speed fluid are taking place. We have performed a limited number of flow visualizations using the injection of a milky white tracer in the near-bed region of a river flow. This technique offers the potential to shed new light on several aspects of the interactions between large-scale turbulent flow structures and between the near-bed and outer regions of the flow in gravel bed-rivers (Roy *et al.* 1999; Roy & Buffin-Bélanger 2001). Figure 16 shows a sequence of images extracted from a video taken in the river reach where the study reported in this paper was conducted. The average flow velocity is $36\,\mathrm{cm\,s^{-1}}$ and flow depth is 28 cm. The tracer was injected directly into the clasts at the bed immediately upstream from the left edge of the images.

This sequence reveals features that have close connections with experimental work in the laboratory. First, we can clearly see the advection of a high-speed flow region immediately followed by a strong upward motion of low-speed fluid from the near-bed

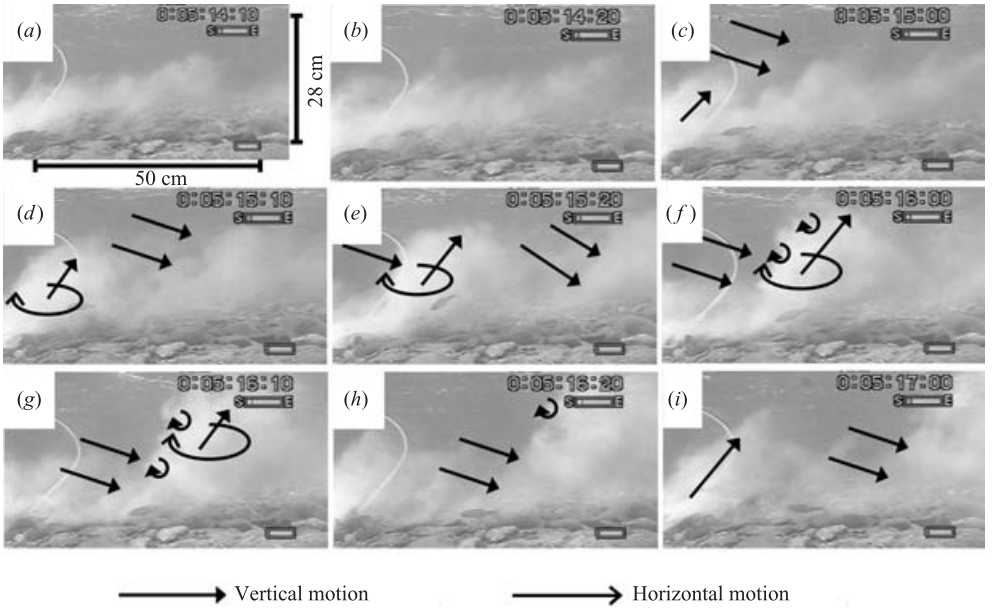

FIGURE 16. Images extracted from a flow visualization sequence in the gravel-bed river. The movement of the white tracer injected at the bed was recorded using an underwater lens linked to a video camera. On the images, flow is moving from left to right at an average velocity of $36\,\mathrm{cm\,s^{-1}}$. The 2.5 s visual sequence illustrates the passage of a high-speed wedge followed by a low-speed wedge which takes the form of a violent ejection.

region. Because of the extent, intensity and suddenness of the vertical expansion of the tracer, such an upward motion is described as a megaburst. The size of this megaburst is well within the values obtained from the space–time velocity matrices and correlations. The violent eruption of low-speed fluid from the bed appears to be triggered by the passage of a large-scale high-speed flow structure that sweeps onto the bed from the outer flow region. The vertical expansion of the tracer occurs at the back of a high-speed wedge. It is noteworthy that once a megaburst has erupted, it takes the shape of a wedge with its front inclined towards the downstream direction. There seems, however, to be little shearing between the wedges as the front of the structure tends to maintain its shape as it advects downstream. These images clearly show how large-scale flow structures can generate intense near-bed turbulence that could in turn help to maintain the sequence of alternating pulses of high- and low-speed pockets. Several authors have suggested that large-scale turbulent structures are critical to the generation of small-scale structures at the wall in turbulent boundary layers above smooth (Pratury & Brodkey 1978; Falco 1991) and rough (Grass *et al.* 1991) boundaries. Our evidence suggests that this mechanism is also occurring in river flows above complex rough boundaries.

Secondly, it is possible to see distinct vortical motions as the structures evolve downstream. The arrows on figure 16 highlight the main flow features and dynamics that could be observed from the images. The vortical motions appear to be formed when flow from the outer region moves towards the bed as evidenced by the white cloud staying close to the near-bed region. Such dynamics give rise to what appears to be a long and narrow streamwise-oriented vortex that shares more similarity with the funnel-shaped vortex described by Kaftori *et al.* (1994) than with the classic hairpin vortex that has been often proposed for this type of flow. This could be the first

evidence that structures analogous to the funnel-shape vortices may develop in a flow over a rough boundary.

Thirdly, the video allowed us to observe the presence of small vortices on the back of the advecting low-speed flow regions. These are also indicated on figure 16. This observation has strong similarity with the model of the outer flow region proposed by Falco (1991). In his model, Falco divided the outer flow region in two important families of motions: typical eddies and the large-scale motions. The typical eddies constitute regions of strong local vorticity. The vortices constantly re-form and redefine the boundaries of the large-scale motions on which they develop. Falco observed these phenomena in flows at a relatively low Reynolds number and he speculated on the possibility of having similar flow patterns at high Reynolds numbers. Hence, it is striking to observe similar flow structures and dynamics in a flow at such a high Reynolds number and above such a complex rough bed.

The approach based on the deployment of an array of current meters used in this study has allowed us to characterize the scales of macro-turbulent flow structures in gravel-bed rivers. The results show that there is a convergence between flume studies over smooth as well as rough beds and our results in a gravel-bed river. There seems to exist a general scaling to describe the macro-turbulent flow structures with outer flow variables and the dynamics observed share many similarities with models derived from laboratory studies. The structures appear to be ubiquitous and dominant features of fluvial turbulent boundary layers. The scales and dynamics of the large-scale flow structures are central to a better understanding of fluvial processes at the river reach scale. Roy & Buffin-Bélanger (2001) have presented an hypothesis suggesting that the large-scale flow structures play a critical role in gravel-bed rivers and that they control much of the turbulence manifestations in the near-bed region as well as in the lee of pebble clusters and obstacles. The large-scale flow structures are even enhanced by a feedback mechanism due to two processes: shedding motions from the lee side of protruding obstacles (Buffin-Bélanger *et al.* 2001) and bursting motions from the near-bed flow region as shown by the flow visualization in this paper. Although it is too early to identify a definite model, the results presented in this paper clearly support such an hypothesis of the turbulent boundary layer in rivers, even with very rough beds. Further deployments in various flow conditions are needed in order to assess fully the variability of the scaling and dynamics of the large-scale flow structures with flow stage.

The authors would like to thank the National Sciences and Engineering Research Council of Canada and the Fonds québécois de la recherche sur la nature et les technologies for their financial support. The comments of three anonymous reviewers were very helpful in improving and clarifying the paper.

REFERENCES

Antonia, R. A., Bisset, D. K. & Browne, L. W. B. 1990 Effect of Reynolds-number on the topology of the organised motion in a turbulent boundary-layer. *J. Fluid Mech.* **213**, 267–286.

Bergeron, N. E. & Abrahams, A. D. 1992 Estimating shear velocity and roughness length from velocity profiles. *Water Resour. Res.* **28**, 2155–2158.

Blackwelder, R. F. 1977 On the role of phase information in conditional sampling. *Phys. Fluids* **20**, s232–s242.

Blackwelder, R. F. & Kovasznay, L. S. 1972 Time scales and correlations in a turbulent boundary layer. *Phys. Fluids* **15**, 1545–1554.

Bogard, D. G. & Tiederman, W. G. 1986 Burst detection with single-point velocity measurements. *J. Fluid Mech.* **162**, 389–413.

Brown, G. L. & Thomas, A. S. W. 1977 Large structure in turbulent boundary layer. *Phys. Fluids* **20**, s243–s252.

Buffin-Bélanger, T. 2001 Structure d'un écoulement turbulent dans un cours d'eau à lit de graviers en présence d'amas de galets. PhD thesis, Département de géographie, Université de Montréal.

Buffin-Bélanger, T. & Roy, A. G. 1998 Effects of a pebble cluster on the turbulent structure of a depth-limited flow in a gravel-bed river. *Geomorphology* **25**, 249–267.

Buffin-Bélanger, T., Roy, A. G. & Kirkbride, A. D. 2000*a* On large-scale flow structures in a gravel-bed river. *Geomorphology* **32**, 417–435.

Buffin-Bélanger, T., Roy, A. G. & Kirkbride, A. D. 2000*b* Vers l'intégration des structures de l'écoulement dans la dynamique d'un cours d'eau à lit de graviers. *Géogr. phys. Q.* **54**, 105–117.

Buffin-Bélanger, T., Roy, A. G. & Levasseur, M. 2001 Interactions entre les structures d'échappement et les structures à grande échelle dans l'écoulement turbulent des rivières à lit de graviers. *Revue des Sciences de l'eau* **14**, 381–407.

Clifford, N. J. 1996 Morphology and stage-dependent flow structure in a gravel-bed river. In *Coherent Flow Structure in Open Channels* (ed. P. J. Ashworth, S. J. Bennett, J. L. Best & S. J. Mclelland), pp. 545–566. John Wiley.

Corino, E. R. & Brodkey, R. S. 1969 A visual investigation of the wall region in turbulent flow. *J. Fluid Mech.* **37**, 1–30.

Defina, A. 1996 Transverse spacing of low-speed streaks in a channel flow over a rough bed. In *Coherent Flow Structure in Open Channels* (ed. P. J. Ashworth, S. J. Bennett, J. L. Best & S. J. Mclelland), pp. 87–99. John Wiley.

Dinehart, R. L. 1999 Correlative velocity fluctuations over a gravel river bed. *Water Resour. Res.* **35**, 569–582.

Falco, R. E. 1977 Coherent motions in the outer region of turbulent boundary layers. *Phys. Fluids* **20**, s124–s132.

Falco, R. E. 1991 A coherent structure model of the turbulent boundary layer and its ability to predict Reynolds number dependence. *Phil. Trans. R. Soc. Lond.* A **336**, 103–129.

Favre, A. J., Gaviglio, J. J. & Dumas, R. 1957 Space–time double correlation and spectra in a turbulent boundary layer. *J. Fluid Mech.* **2**, 313–341.

Ferguson, R. I., Kirkbride, A. D. & Roy, A. G. 1996 Markov analysis of velocity fluctuations in gravel-bed rivers. In *Coherent Flow Structure in Open Channels* (ed. P. J. Ashworth, S. J. Bennett, J. L. Best & S. J. Mclelland), pp. 165–183. John Wiley.

Ferro, V. & Baiamonte, G. 1992 Flow velocity profiles in gravel-bed rivers. *J. Hydraul. Engng* **120**, 60–80.

Folk, R. L. 1974 *Petrology of Sedimentary Rocks*, 2nd Edn. Hemphill's, Austin.

Grass, A. J. 1971 Structural features of turbulent flow over smooth and rough boundaries. *J. Fluid Mech.* **50**, 233–255.

Grass, A. J. & Mansour-Tehrani, M. 1996 Generalized scaling of coherent bursting structures in the near-wall region of turbulent flow over smooth and rough boundaries. In *Coherent Flow Structure in Open Channels* (ed. P. J. Ashworth, S. J. Bennett, J. L. Best & S. J. Mclelland), pp. 41–61. John Wiley.

Grass, A. J., Stuart, R. J. & Mansour-Tehrani, M. 1991 Vortical structures and coherent motion in turbulent flow over smooth and rough boundaries. *Phil. Trans. R. Soc. Lond.* A **336**, 29–47.

Guezennec, Y. G., Piomelli, U. & Kim, J. 1989 On the shape and dynamics of wall structures. *Phys. Fluids* **1**, 764–766.

Imamoto, H. & Ishigaki, T. 1987 Visualization of longitudinal eddies in an open channel flow. In *Flow Visualisation IV* (ed. C. Véret), pp. 333–337. Hemisphere.

Jackson, G. 1976 Sedimentological and fluid-dynamic implications of the turbulent bursting phenomenon in geophysical flows. *J. Fluid Mech.* **77**, 531–560.

Kaftori, D., Hetsroni, G. & Banerjee, S. 1994 Funnel-shaped vortical structures in wall-turbulence. *Phys. Fluids* **6**, 3035–3045.

Kim, K. C. & Adrian, R. J. 1999 Very large-scale motion in the outer layer. *Phys. Fluids* **11**, 417–422.

Kline, S. J., Reynolds, W. C., Schraub, F. A. & Rundstadler, P. W. 1967 The structure of turbulent boundary layer. *J. Fluid Mech.* **30**, 741–773.

Kirkbride, A. D. & Ferguson, R. I. 1995 Turbulent flow structure in a gravel-bed river: Markov chain analysis of the fluctuating velocity profile. *Earth Surface Processes and Landforms* **20**, 721–733.

Kirkgöz, M. S. 1989 Turbulent velocity profiles for smooth and rough open channel flow. *J. Hydraul. Engng* **115**, 1543–1561.

Komori, S., Murakami, Y. & Ueda, H. 1989 The relationship between surface-renewal and bursting motions in an open-channel flow. *J. Fluid Mech.* **203**, 103–123.

Krogstad, P. Å, Antonia, R. A. & Browne, W. B. 1992 Comparison between rough- and smooth-wall turbulent boundary layers. *J. Fluid Mech.* **245**, 599–617.

Krogstad, P. Å., Kaspersen, J. H. & Rimestad, S. 1998 Convection velocities in turbulent boundary layers. *Phys. Fluids* **10**, 949–957.

Lapointe, M., De Serres, B., Biron, P. M., Roy, A. G. 1996 Using spectral analysis to detect sensor noise and correct turbulence intensity and shear stress estimates from EMCM flow records. *Earth Surface Processes and Landforms* **21**, 195–203.

Laufer, J. 1975 New trends in experimental turbulent research. *Annu. Rev. Fluid Mech.* **7**, 307–326.

Lawless, M. & Robert, A. 2001 Scales of boundary resistance in coarse-grained channels: turbulent velocity profiles and implications. *Geomorphology* **39**, 221–238.

Liu, Z., Adrian, R. J. & Hanratty, T. J. 2001 Large-scale mode of turbulent channel flow: transport and structure. *J. Fluid Mech.* **448**, 53–80.

Luchik, T. S. & Tiederman, W. G. 1987 Timescale and structure of ejections and bursts in turbulent channel flows. *J. Fluid Mech.* **174**, 529–552.

Matthes, G. H. 1947 Macroturbulence in natural stream flow. *Trans. AGU* **28**, 255–265.

Nakagawa, H. & Nezu, I. 1981 Structure of space–time correlations of bursting phenomena in an open-channel flow. *J. Fluid Mech.* **104**, 1–43.

Nelson, J. M., Shreve, R. L., McLean, S. R. & Drake, T. G. 1995 Role of near-bed turbulence structure in bed load transport and bed form mechanics. *Water Resour. Res.* **31**, 2071–2086.

Nezu, I. & Nakagawa, H. 1993 *Turbulence in Open-Channel Flows*. A. A Balkema.

Nikora, V. & Goring, D. 2000 Eddy convection velocity and Taylor's hypothesis of 'frozen' turbulence in a rough-bed open-channel flow. *J. Hydrosci. Hydraul. Engng* **18**, 75–91.

Nikora, V. I. & Smart, G. M. 1997 Turbulence characteristics of New Zealand gravel-bed rivers. *J. Hydraul. Engng* **123**, 764–773.

Niño, Y. & Garcia, M. H. 1996 Experiments on particle-turbulence interactions in the near-wall region of an open channel flow: Implications for sediment transport. *J. Fluid Mech.* **326**, 285–319.

Offen, G. R. & Kline, S. J. 1975 A proposed model of the bursting process in turbulent boundary layers. *J. Fluid Mech.* **70,** 209–228.

Papanicolaou, A. N., Diplas, P., Dancey, C. L. & Balakrishnan, M. 2001 Surface roughness effects in near-bed turbulence: implications to sediment entrainment. *J. Engng Mech.* **127**, 211–218.

Piomelli, U., Ballint, J.-L. & Wallace, J. M. 1989 On the validity of Taylor's hypothesis for wall-bounded flows. *Phys Fluids* A **1**, 609–611.

Pratury, A. K & Brodkey, R. S. 1978 A stereoscopic visual study of coherent structures in turbulent shear flow. *J. Fluid Mech.* **89**, 251–272.

Robert, A. 1997 Characteristics of velocity profiles along riffle-pool sequences and estimates of bed shear stress. *Geomorphology* **19**, 89–98.

Robert, A., Roy, A. G. & De Serres, B. 1992 Changes in velocity profiles at roughness transition in coarse-grained channels. *Sedimentology* **39**, 725–735.

Robert, A., Roy, A. G. & De Serres, B. 1993 Space–time correlations of velocity measurements at a roughness transition in a gravel-bed river. In *Turbulence: Perspectives on Flow and Sediment Transport* (ed. N. J. Clifford, J. R. French & J. Hardisty), pp. 165–184. John Wiley & Sons, Chichester.

Robert, A., Roy, A. G. & De Serres, B. 1996 Turbulence at a roughness transition in a depth-limited flow over a gravel-bed river. *Geomorphology* **16**, 175–187.

Robinson, S. K. 1991 Coherent motions in the turbulent boundary layer. *Annu. Rev. Fluid Mech.* **23**, 601–639.

Roy, A. G., Biron, P. M., Buffin-Bélanger, T. & Levasseur, M. 1999 Combined visual and quantitative techniques in the study of natural turbulent flows. *Water Resour. Res.* **35**, 871–877.

Roy, A. G., Biron, P. M. & Lapointe, M. F. 1997 Implications of low-pass filtering on power spectra and autocorrelation functions of turbulent velocity signals. *Math. Geol.* **29**, 653–668.

Roy, Y. M. & Blackwelder, R. F. 1994 On the role of the outer region in the turbulent-boundary-layer bursting process. *J. Fluid Mech.* **259**, 345–373.

Roy, A. G. & Buffin-Bélanger, T. 2001 Advances in the study of turbulent flow structures in gravel-bed rivers. In *Gravel-Bed River V* (ed. M. Paul Mosley), pp. 375–397. New Zealand Hydrological Society.

Roy, A. G., Buffin-Bélanger, T. & Deland, S. 1996 Scales of turbulent coherent flow structures in a gravel bed river. In *Coherent Flow Structure in Open Channels* (ed. P. J. Ashworth, S. J. Bennett, J. L. Best & S. J. Mclelland), pp. 147–164. John Wiley.

Schvidchenko, A. B. & Pender, G. 2001 Macroturbulent structure of open-channel flow over gravel beds. *Water Resour. Res.* **37**, 709–719.

Shah, D. A. & Antonia, R. A. 1989 Scaling of the 'bursting' period in turbulent boundary layer and duct flows. *Phy. Fluids* A **1**, 318–325.

Smart, G. M. 1999 Turbulent velocity profiles and boundary shear in gravel-bed rivers. *J. Hydraul. Engng* **125**, 106–116.

Smart, G. 2001 Discussion on Advances in the study of turbulent flow structures in gravel-bed rivers. In *Gravel-Bed River V* (ed. M. Paul Mosley), p. 399. New Zealand Hydrological Society.

Soulsby, R. L. 1980 Selecting record length and digitization rate for near bed turbulence measurements. *J. Phys. Oceanogr.* **10**, 208–219.

Tamburrino, A. & Gulliver, J. S. 1999 Large flow structures in a turbulent open channel flow. *J. Hydraul. Res.* **37**, 363–380.

Yalin, M. S. 1992 *River Mechanics*. Pergamon.

Zaman, K. B. M. Q. & Hussain, A. K. M. F. 1981 Taylor hypothesis and large-scale coherent structures. *J. Fluid Mech.* **112**, 379–396.